ORIGINAL RESEARCH ARTICLE

ENHANCED IMPINGEMENT JET COOLING OF GAS TURBINE WALL HEAT TRANSFER USING CFD CHT CODE: INFLUENCE OF WALL THERMAL GRADIENT WITH FIN AND DIMPLE OBSTACLES

A. M. El-Jummah[1*]., G. E. Andrews[2] and J. E. J. Staggs[2]

([1]Department of Mechanical Engineering, University of Maiduguri, P. M. B. 1069, Nigeria
[2]School of Chemical and Process Engineering, University of Leeds, LS2 9JT, United Kingdom)
*Corresponding author's e-mail address: al-jummah@hotmail.com

ABSTRACT

Gas turbine (GT) jet cooling using the regenerative or impingement jet backside cooling system is applicable to low NO_x GT combustors and was investigated in the present work. The impingement heat transfer investigated is for the techniques where all the combustion air is used for wall cooling prior to passing through the flame stabiliser. Ten rows of impingement holes were modelled and are for four different types of obstacles: rectangular-pin in co- and cross-flows, circular pin-fin in cross-flow and dimple in direct-flow configurations, arranged in the impingement jet air flow direction. Conjugate heat transfer (CHT) and computational fluid dynamics (CFD) techniques were combined and applied in the computational analysis. Only the two obstacles in rectangular shape: co- and cross-flow configurations were validated against experimental results, as the other two has no experimental data available, but similar CFD methodology was applied. The impingement jet cooling enhancing obstacles were aligned transverse to the direction of the impingement jet cross-flow on the target surface and were equally spaced on the centre-line between each row of jet holes transverse to the cross-flow. Also, one heat transfer obstacle was used per impingement jet air flow in order to see the level of heat transfer augmentation of each one. The CFD calculations were carried out for an air mass flux G of 1.08, 1.48 and 1.94 kg/sm^2bar, hence for each obstacle grid geometry, three computations were conducted and therefore a total of twelve different computations for this investigation. These high mass flux used, are only applicable to the regenerative combustor wall cooling applications. Validation of the CFD predictions with the experimental data indicates good agreement for impingement gap flow pressure loss ($\Delta P/P$) and the surface average heat transfer coefficient (HTC), h. Other predictions were also carried out and were for locally average X^2 HTC, hole exit pressure loss, turbulence kinetic energy (TKE), flow-maldistribution, Nusselt number (Nu) and normalized temperature, T^* or thermal gradient. It was concluded here that the rectangular-pin obstacles have the highest exit hole and impingement gap pressure loss, but with low heat transfer as a result of higher flow-maldistribution. Dimple obstacle has the lowest heat transfer, but is because most of the heat is taken away (or sucked in) by the dimple pot. The main effect of the obstacles was to increase the heat transfer to the impingement jet surface, but the dimple surface was predicted to have a very poor performance, with significantly reduced target wall heat transfer and thermal gradient.

1.0   Introduction

The low NO_x primary zone combustor wall cooling requires the type of impingement geometry investigated (Figure 1a) in this present work, as high coolant mass flow rate, G (kg/sm^{2}bar) with a low coolant pressure loss is the major requirement. Sufficient air pressure must be available after the wall cooling, which is in order to overcome the pressure loss at the low NO_x flame stabilizer for flame stability and fuel/air mixing procedures. Hence high velocity cross-flow interactions should be avoided with the obstacles along the cross-flow direction to combat high coolant pressure loss. Abdul Husain and Andrews (1991) reviewed the use of obstacles to enhanced impingement heat transfer, it shows that most work had investigated the enhancement experimentally. The maximum heat transfer enhancement found experimentally was 20 - 50% using several pin-fins between the impingement jets.

The present CHT CFD work (Figure 1b) investigates four main heat transfer enhancing obstacles: rectangular-pin (co- and cross-flows), pin-fin (cross-flow) and dimple (direct flow) configurations, with only two that have been experimentally investigated: rectangular-pin (co- and cross-flow), as in Figure 1c and d. El-jummah et al. (2014a, 2017, 2018) validated the computational methods used in the present work against experimental results,   they investigated experimentally flat ribs and rectangular fins or slotted ribs: co- and cross-flows of the coolant in the impingement gap, as used in this work. The predictions were in good agreement with the experimental mean surface averaged HTC and pressure loss, which is the reason why the present work is adopting the methodology employed. The pressure loss agreement found in their work indicates that the aerodynamic predictions were correct. Therefore, the present CHT CFD research, applies the same computational procedures to validate the results and to explore the possible design options for enhanced impingement cooling heat transfer applications.

The impingement jet hole size D, pitch X, and gap Z, in this work were the same as for the smooth target impingement wall (El-jummah et al., 2014a) as well as for previous predictions of impingement cooling with obstacles in the gap (El-jummah et al., 2016a, 2017, 2018). A 10 × 10 array of impingement jet holes was used with a fixed X/D, Z/D and n, as summarised in Table 1 (El-jummah et al., 2013, 2016a, b). The G used are from 1.08 - 1.93 kg/sm^{2}bar, the same as used by El-jummah et al. (2013) for the smooth wall. Each coolant G requires a new computation, with slight changes in the impingement gap grid refinement. Also, a new computational grid as in Figure 2 and Table 2 is necessary for each obstacle that will be predicted, as the effect of obstacles in the impingement gap as in Table 3 will be investigated. Table 2 shows that a fixed obstacle height H to width W ratio of 0.93 (El-jummah et al., 2016a, 2017, 2018) for all the rectangular (thickness, t of 3 mm) and circular (thickness, t = W = Do = 8.59 mm) pins was used and depth δ to diameter Do (or t) ratio of 0.30 for the dimple obstacle was used. The dimple depth was taken based on work by Xie et al. (2013) and the diameter (or width) is based on work by El-jummah et al. (2017), which is in order that the obstacles have similar geometrical properties.

2.   Computational Methods

2.1   Model Grid Geometry

The grid model geometry is shown in Figure 2, which was created based on the computational domain shown in Figure 1b and is the same as that modeled in the work of El-jummah et al. (2016a, 2018) and Xie et al. (2013) for smooth target geometry of Table 1.   This work

315

Corresponding author's e-mail address: al-jummah@hotmail.com

investigates the potential improvement in the heat transfer using the obstacles in the impingement gap of Table 2. The dimensions of the obstacles are shown in Figure 2 and Table 2. The rectangular and circular pin-fins had a height H that is 80 % of Z with equal pin width W. The dimple in the impingement gap in Figure 1 offers no obstruction to the cross-flow, but changes the interaction of the impingement jet with the target surface, as the impingement jet was aligned with the dimple. These obstacles were investigated for the cross-flow normal to the obstacles. The gap between the top of the rectangular and circular pin-fins was to allow for thermal expansion, as the wall and rib are hotter than the impingement jet wall (El-jummah et al., 2018). If there was a solid connection, differential thermal expansion could create thermal stresses and cracking.

The computational grid geometries as summarized in Table 3, were modeled using ANSYS ICEM meshing tool. The dimpled obstacle of Figure 2 penetrates through the depth of the target wall, which makes the fluid grids of the impingement gap to replace part of the solid wall grids. It also increased the impingement gap cell size and reduced the target wall cells, as a proportion of the total computational cells, as in Table 3. The grid geometries employed symmetrical approach as in Figure 1b and 2, where half holes and half obstacles along the row of holes as in Figure 2 were modeled. Also, all the obstacles used were over a million computational nodes and the number of cells in the plenum was fixed at 35.3 % of the total grids and was shown to be adequate (El-jummah et al., 2013a, b, 2016a). The dimpled target surface was modeled with the dimples in - line with the impingement air jets, hence air jet could flow directly through the dimple. The other obstacles grids were in the gap, hence the obstacle solid walls replaced part of the gap fluid grid as in Table 3.
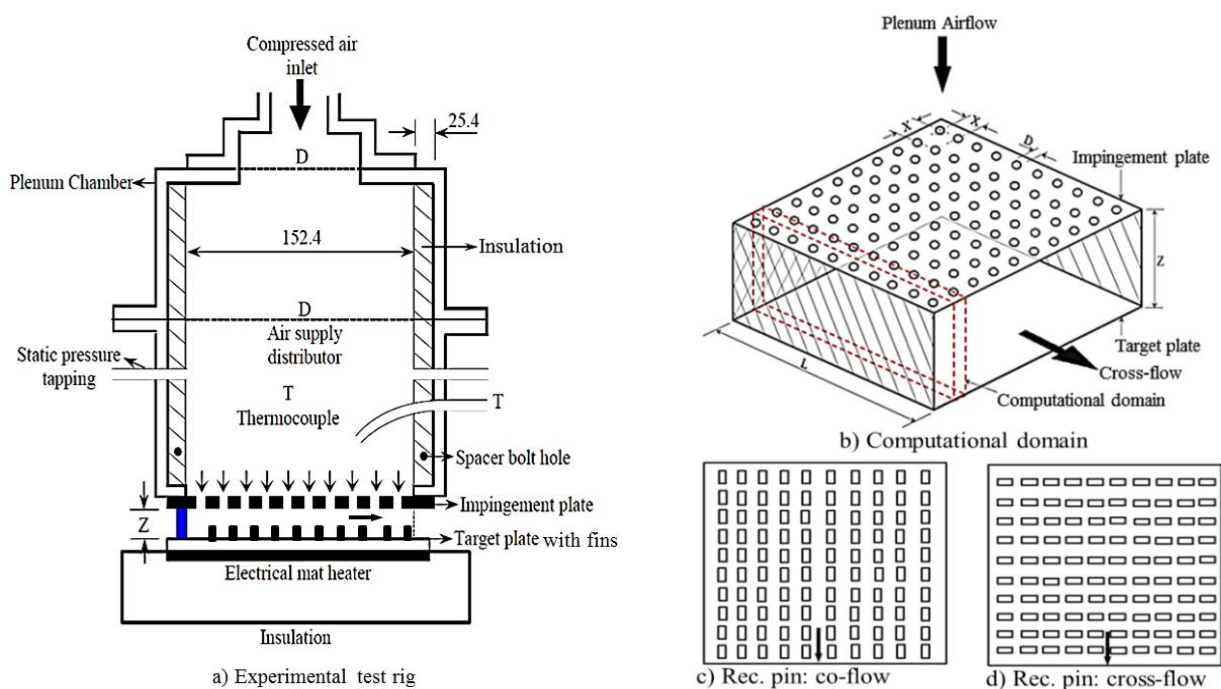
Figure 1: Schematic diagrams of the impingement jet cooling geometries and obstacle test walls

Table 1: Geometrical Parameters

Variables	Dimensions
D (mm)	3.27
X (mm)	15.24
Z (mm)	10.00
L (mm)	6.35
L/D	1.94
X/D	4.66
Z/D	3.06
X/Z	1.52
n	4306 m^{-2}
Array	10 × 10
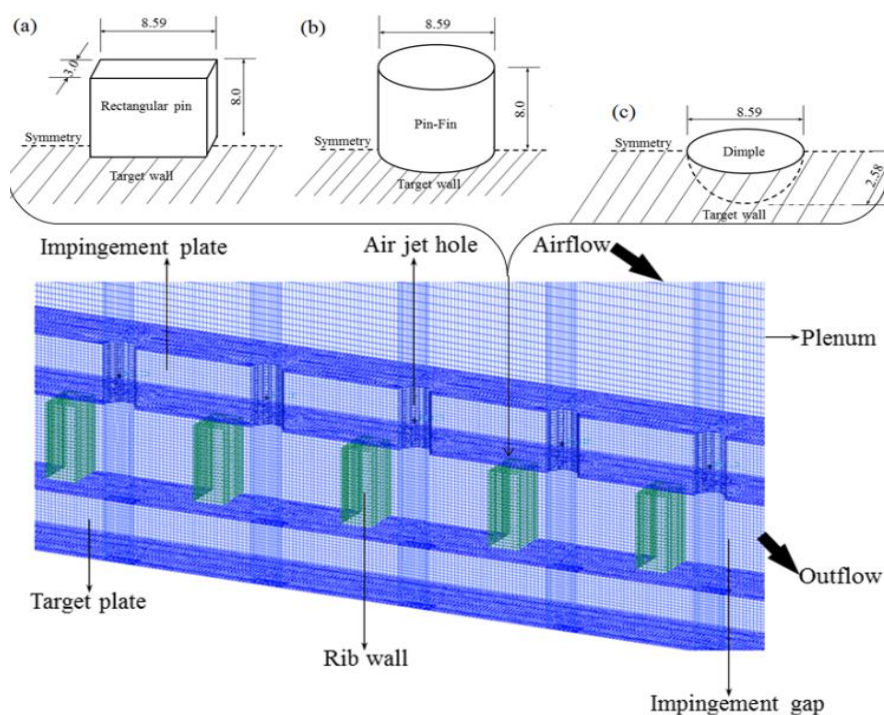
Figure 2: The impingement grid model geometry with rec. pin in cross-flow on the target surface

Table 2: Obstacle Walls Parameters

Types	W or Do (mm)	H or δ (mm)	t (mm)	H/W δ/Do
Rec. pin: co-flow	8.59	8.00	3.00	0.93
Rec. pin:cross-flow	8.59	8.00	3.00	0.93
Pin-fin (circular)	8.59	8.00	8.59	0.93
Dimple: direct flow	8.59	2.58	8.59	0.30

Corresponding author's e-mail address: al-jummah@hotmail.com

Table 3: Grid node distribution for y+ ~35

Types	Grid node distribution (%)			
	Test walls	Obstacles	Gap	Holes
Rec. pin: co-flow	28.5	8.3	19.5	8.4
Rec. pin: cross-flow	28.5	8.3	19.5	8.4
Pin-fin (circular)	26.5	6.7	23.4	8.1
Dimple	22.8	5.7	27.4	8.8

2.2   Computational Procedures

Computations were carried out for four obstacle walls using G of 1.08, 1.48 and 1.98 kg/sm^{2}bar, as Table 4: computational boundary flow conditions, shows and were the same flow conditions used by El-jummah et al. (2013, 2016a, 2017, 2018). The ANSYS Fluent commercial code was used in running the calculation of the twelve grids modelled geometries (for the four obstacles) and was computed using standard k - ε turbulence. Wall function y+ value ~35 (El-jummah et al 2014a, 2017), as Table 3 shows was applied, the values of which were reported to be within the near wall range of 30 < y+< 300 law of the wall. This computational procedure was the same as that previously validated (El-jummah et al., 2013, 2014a), as grid sensitivity (El-jummah et al 2014a) was also adequately performed. The test indicates that for grid size greater than half a million, there was little improvement in the predictions relative to the measured data, hence the distribution of nodes as summarised in Table 3 and as shown in Figure 2.

The standard k - ε model has been shown to better predict the flow aerodynamics in the impingement gap, which include strong flow recirculation as well as the flow separation and reattachment (El-jummah et al., 2015a) in the jet holes. Also, the modelled grids shown in Figure 2 for all the obstacle geometries have minimum cell orthogonal quality and aspect ratio fixed at 0.61 and 3.53, respectively. The convergence criteria were set at 10^{-5} for continuity, 10^{-11} for energy and 10^{-6} for k, ε and momentum: x, y and z velocities. The second order and first order discretization schemes for the momentum and TKE/dissipation were applied, also PISO schemes that were based on PRESTO applications was used.

3.   Predicted Results

3.1   Validation Case

The requirement to validate this CHT CFD investigation was based on the fact that measured pressure loss (ΔP/P) and surface average heat transfer (HTC) data, are available for two obstacles: rectangular pins, as Figures 3 and 4 shows respectively. Figure 3 compares the predicted pressure loss against G of the rectangular pins of co-flow and cross-flow obstacles, both shows good agreement with the experimental data. This indicates that the aerodynamics were adequately predicted, which also assert that the flow-maldistribution and hole pressure loss could be predicted correctly. Also shown is the comparison of the predicted surface average HTC using Equation 1 below with measured data, as in Figure 4. Both pins predicted surface average HTC agrees with the measurement, even though the cross-flow obstacle slightly falls close to the error bar, but is within the acceptable requirement. Abdul Husain and

Andrews (1991) showed that the heat transfer error of ± 10 should be acceptable, hence the data is correct.

The aerodynamics in the impingement gap are complex (Goldstein et al., 1982), as shown by El-jummah et al. (2013a, 2018) using CHT CFD modelling procedures. The additions of obstacles to the target wall was aimed at enhancing the heat transfer and were placed at the location of the reverse flow (Goldstein et al., 1982) between each impingement jet. The inclusion of the obstacle increases the complexities of the aerodynamics, as the cross-flow increases with successive rows of impingement jets. This flow complexity is shown as velocity path-lines by Authors previous work by El-jummah et al. (2015a, 2016a, b, 2018) and were compared with smooth target geometrical predictions. Their comparison showed the aerodynamics complexity increases with addition of obstacles, which were placed to have convective heat transfer from the reversed jet flow at certain upstream few holes. This complex phenomena requires that CFD invesgigations are initiated and should be validated.

$$h = \frac{q''}{(T_s - T_\infty)} \qquad (1)$$

Table 4: Boundary Flow Conditions

G (kg/sm^{2}bara)	1.93	1.48	1.08
Vj (m/s)	43.41	33.5	24.3
Uc (m/s)	24.0	18.4	13.4
Vj/Uc	1.8	1.8	1.8
Re$_h$ $(= \rho V_j D / \mu)$	9680	7440	5400
T$_\infty$(K)	288	288	288
Tw(K)	353	353	353
ρ (kg/m^3)	1.225	1.225	1.225
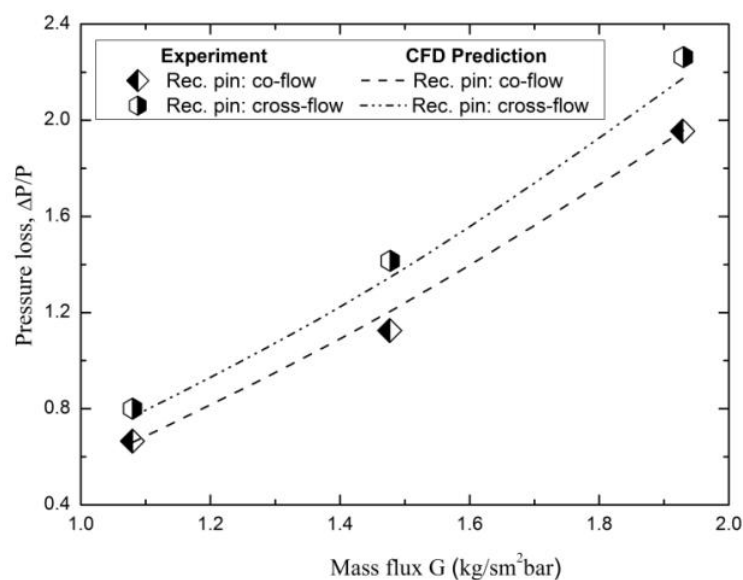
Figure 3: Comparison of measured pressure loss with CFD predicted data for varied

Corresponding author's e-mail address: al-jummah@hotmail.com
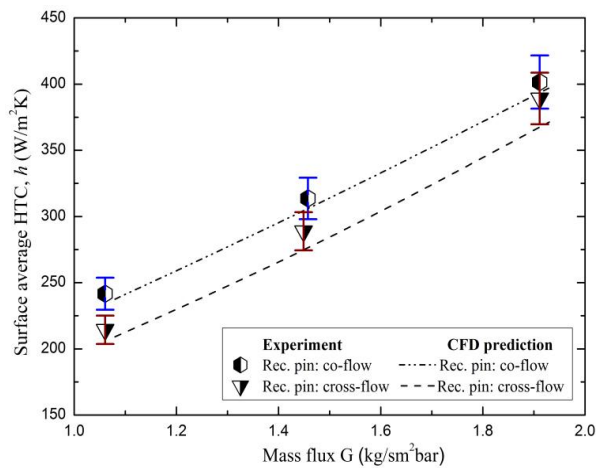
Figure 4: Comparison of experimental surface average HTC with predicted data for varied G
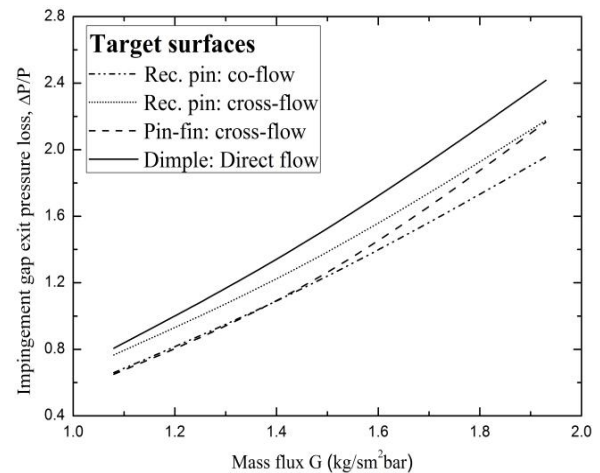
Figure 5: CFD predicted pressure loss for all the modelled obstacles and for varied G

3.2 Prediction of the Overall/Axial Pressure loss and Flow-Maldistribution

Experimentally, the pressure loss results for a smooth wall have been shown previously to have good agreement with the CHT CFD predictions, using the present computational methods (El-jummah et al. 2014a, b). To achieve this agreement, the experimental measurement configuration had to be modelled precisely. In the experiment, the impingement cooled duct had a discharge length of 25 mm before discharge to the atmosphere, as in Figure 1a. On three sides this flange was used to bolt the test section to the impingement wall with the spacer gap, Z and this also sealed the gap from air leaks on three sides. On the flow exit side as in Figure 1b, no bolts were present and the gap was open. The extended outlet region is included in the modelling (Figure 2) and predictions.

Figure 5 shows that there was flow expansion to the full width of the duct with associated static pressure recovery in the 25 mm outlet section. This was particularly strong for the cross-flow obstacles and the impact of the cross-flow in the impingement gap is to induce a flow-maldistribution between the first and last impingement holes. Figure 5 shows the predicted pressure loss for the range of G, for all the four obstacles along the impingement gap exit flow.
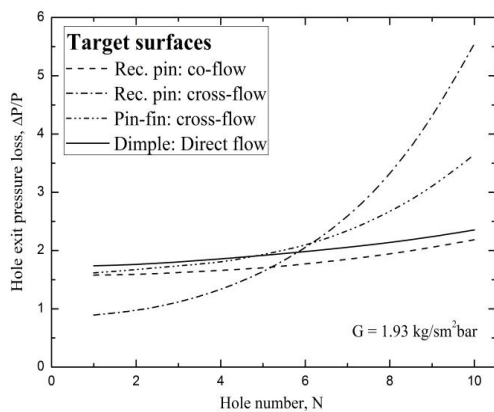
Figure 6: Predicted jet exit hole pressure loss for all the modelled obstacles at the highest G
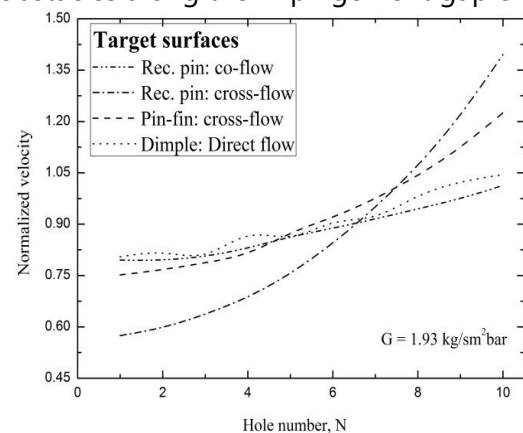
Figure 7: Flow-maldistribution in the jet holes for all the modelled obstacles at the highest G

Comparison of all the four obstacles indicates that the higher the G, the higher is the pressure loss at the exit gap. Also, it shows that the dimple obstacle has higher pressure loss at the exit gap and is followed by the rectangular pin in cross-flow and with similar trend, which is expected. This is because all the jets air entrained within the array of the obstacles are now forced to exit at the same time, which are at higher exit velocity. Worthy of knowing is that the other two pin obstacles have almost the same pressure loss and with similar trend. This should be because, the trend of jets movement (recirculation) along the gap is closely in the same phase, as the range of G and geometries are also the same. Although at the highest G, the circular pin in cross-flow has higher pressure loss which is close to that for rectangular pin in cross-flow. This indicates that with the highest G, flow recirculation increases along the gap for the pin-fin, which at exit stage generate higher velocity.

The prediction of the axial variation of the pressure loss across the impingement jet wall in Figure 6, were determined as the difference in the plenum chamber air supply static pressure and the impingement wall static pressure. This is the static pressure between adjacent impingement holes for the same axial location. At the last hole this did not include the flow expansion downstream and static pressure recovery in the outlet duct. The obstacles create a blockage to the cross-flow which was predicted to inpact on the pressure loss (Figure 6). Figure 6 shows the axial hole exit pressure loss for all the obstacles and for the highest G, with the rectangular pin in cross-flow generating the highest exist pressure loss. The circular pin fins have the next greatest impact, even though they leave a clear gap between the pins. The trend of the rectangular pin in co-flow and that for the dimple as Figure 6 show is the same, with only a slight increased demonstrated by the co-flow obstacle. This is expected for both as both had their jet flow concentrated upstream the impingement jet holes, but with the impingement gap cross-flow, the air outflow dominates at the exit gap. This behaviour have been shown to be similar to that exhibited by the smooth target surface, hence the two obstacles are not expected to produce much significant heat transfer.

Flow-maldistribution is the characteristic of the air jet-flow through the holes and the impingement gap as a result of cross-flow, which is also controlled by the size of G used. Also, the impact of the flow-maldistribution is proportional to the pressure loss, as Figures 6 and 7 shows. Figure 7 shows that the similarity situation demonstrated by the cross-flow obstacles for the pressure loss in Figure 6 is also seen here. This is also the same with the co-flow and dimple obstacles but with haphazard behaviour demonstrated by the dimple one as there is no increased in the cross-flow blockage and for the co-flow the blockage is insignificant between obstacles.

Figure 7 show that the greater flow reversal and reduced target surface flow, must give a greater resistance to the impingement cross-flow. This then increases the flow-maldistribution along the impingement gap for all the obstacles, as turbulence is also generated significantly.

3.3   Predictions of the Turbulent Kinetic Energy and Nusselt Number Profiles

The turbulent kinetic energy (TKE) on the wall surface controls the wall heat transfer (El-jummah et al., 2013, 2014a, 2019). Figure 8 (left: a - d) shows the predicted TKE in the symmetrical plane in line with the impingement jets for the obstacles and compares them with the predicted Nusselt number, Nu using Equation 2 (by the right (a - d) hand side). Figure 8 shows that the action of the obstacle is to reduce the turbulence on the surface and to move the peak turbulence to the obstacle surface (El-jummah et al., 2019). The only surface roughness

Corresponding author's e-mail address: al-jummah@hotmail.com

(obstacle) that increases turbulence on the target wall is the dimple target surface and is deflected out of the dimple by the cross-flow, as Figure 8 show. Figure 8 also show that for the rectangular pin in co-flow and pin-fin obstacles, there is significant increase of TKE on the target surface which also improves on their heat transfer as Figure 8 (right: a and c) shows. Figure 8 also show that the cross-flow rectangular pin that is expected to generate higher turbulence on the target surface, hence heat transfer demonstrate lower value for both TKE and Nu. This is expected, as most of the jet air is reversed back to the impingement jet surface as will be seen later using Equation 3 that it increases the heat there. Figure 8 (right) for all obstacles is very similar to that for the distribution of TKE in Figure 8 (left), which further explains the control of TKE in enhancing the heat transfer.
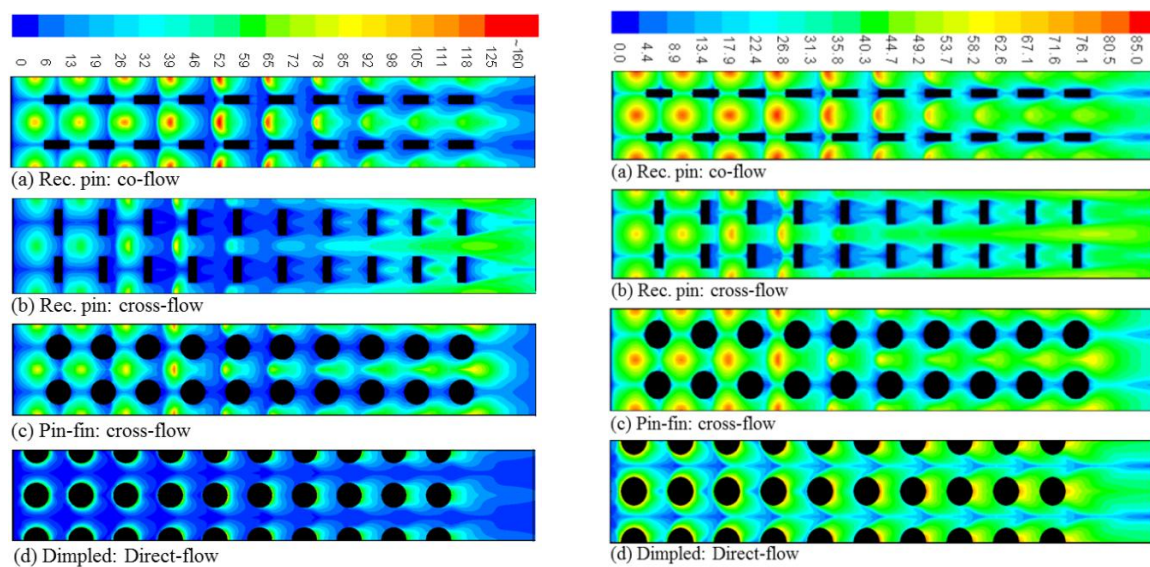
Figure 8: Contour of TKE (left) and Nusselt number (right) on target surface for the highest G
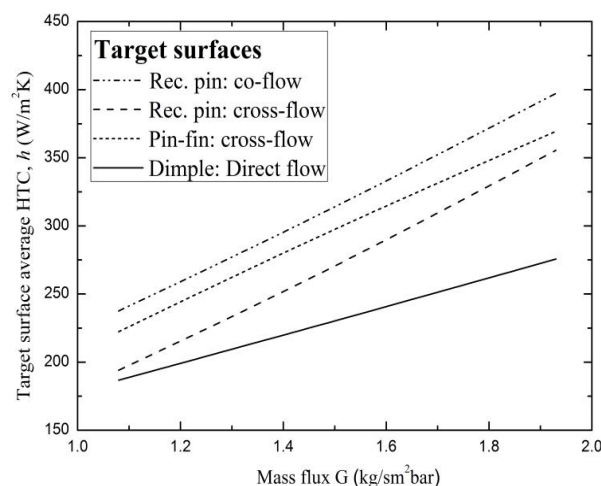
Figure 9: The predicted surface average HTC on the enhanced target surfaces for varied G

$$Nu = \frac{hD}{k_f} \qquad (2)$$
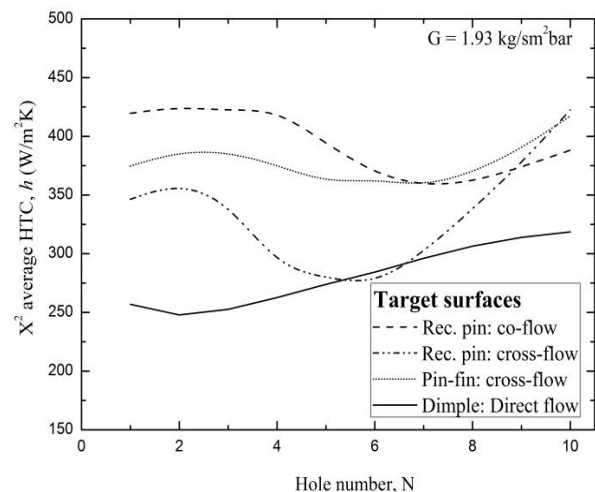
Figure 10: The predicted X^2 average HTC on the enhanced target surface for the highest G

$$T^* = \frac{(T - T_\infty)}{(T_w - T_\infty)} \qquad (3)$$

3.4 The Surface and X^2 Average HTC for varied G

The work by El-jummah et al. (2016a, 2017, 2018, 2019) and that of Figure 4 above, for the surface average HTC with impingement heat transfer have shown good agreement between measurements and predictions, using the same methodology as in this work. Figures 9 and 10 are the results for the surface and X^2 (or local) average HTC on the whole length of the target surface for varied G and on the axial X^2 trends of the surface, respectively. All the obstacles showed increased in surface HTC with G with the co-flow obstacle given the highest but had the worse local HTC, as in Figure 7. This is because at the first six holes there was local HTC deterioration, then from hole 7 insignificant improvement downstream was then seen upstream the cross-flow gap. Part of the reason for this worse prediction in X2 HTC was the flow-maldistribution shown in Figure 7. The extra cross-flow pressure loss created by the obstacles, caused the first four impingement holes to have lower air mass flow than the last four and is the ideal. This reduces the heat transfer for the first four holes and increases it for the last four holes, with little changes in the X^2 average HTC. Even though for the dimple, there was significant increased downstream the holes but it has the lowest HTC, which was the result of the pressure loss shown in Figure 6. Another reason for the deteriorated surface average HTC was due to the dimple increasing the reverse flow of the jets and deflecting the jets away from the cooled surface Also, there was only a small axial gradient in the local HTC with a small increase in the downstream part of the cross-flow. Hence the dimpled surface has worse local HTC at all axial locations and for the surface HTC than the other three obstacles. The circular pin-fins in cross-flow, also had higher local HTC upstream but with reduced HTC downstream, which is expected base on the trend demonstrated by the flow-maldistribution above.

(a) Rectangular pin: co-flow

(b) Rectangular pin: cross-flow

(c) Pin-fin: cross-flow

(d) Dimple: direct-flow

(a) Rectangular pin: co-flow

(b) Rectangular pin: cross-flow

(c) Pin-fin: cross-flow

(d) Dimple: Direct-flow
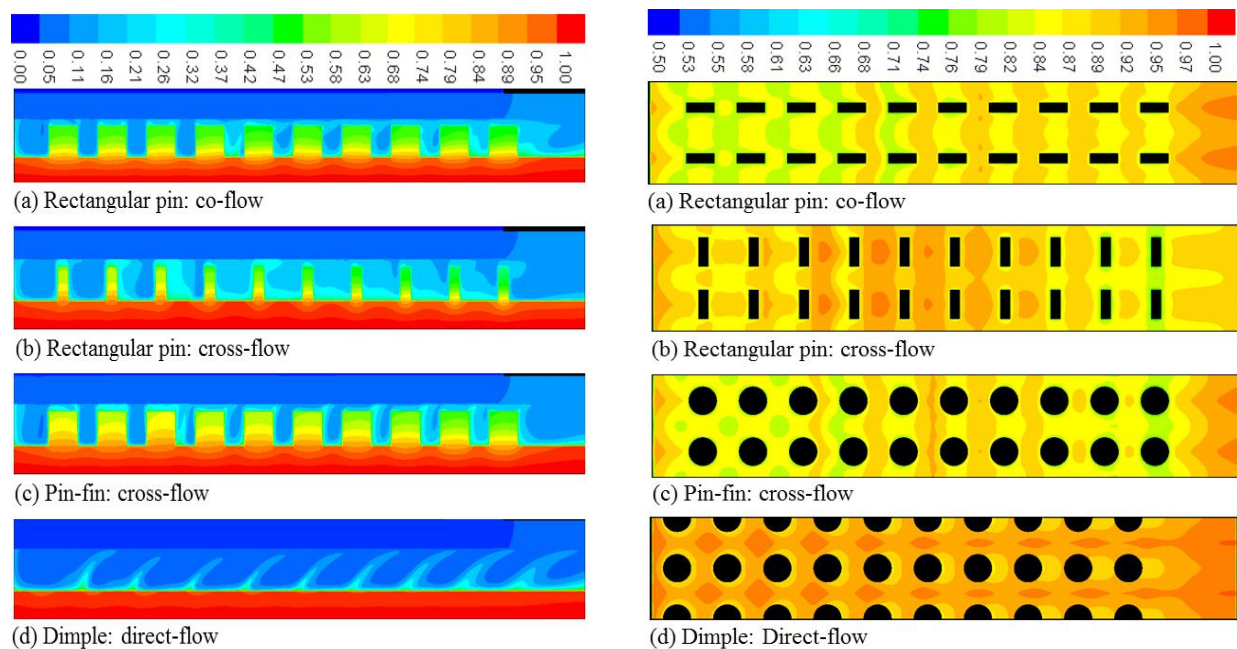
Figure 11: Contours of CFD predicted normalized temperature in the impingement gap (left) and on the target surface (right) for the highest G of 1.93 kg/sm^{2}bar

Corresponding author's e-mail address: al-jummah@hotmail.com
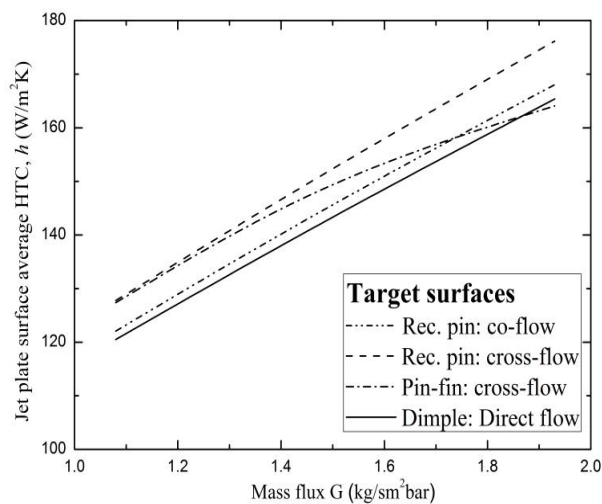
Figure 12: The predicted surface average HTC on the impingement jet surfaces for varied G
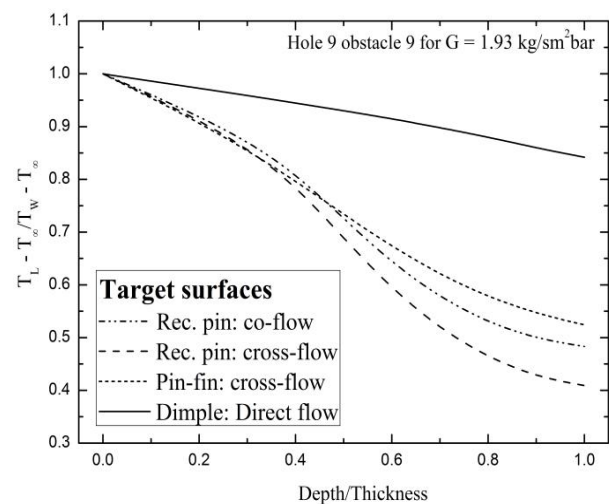
Figure 13: The predicted normalized thermal gradient on the target surface for highest G

For the first four holes, all the obstacles were predicted to have much higher local surface average heat transfer, this was 50% higher than for the dimpled surface and 20 % lower for the cylindrical pin-fins. The main benefit of the obstacles was in the downstream part of the cross-flow in the impingement gap. This is when the cross-flow velocity had increased, due to the flow outlet from the upstream jets and higher velocity impingement jets were created due to flow-maldistribution. However, this downstream velocity increased was never sufficient to overcome the large deterioration in HTC for the first four holes. Part of the reason for this was the worse flow-maldistribution, so that the first holes had less air than the downstream holes and this kind of maldistribution was worse with obstacles as compared with the smooth wall (El-jummah et al. 2018). Recall that when obstacles are placed between the holes, surface interaction is terminates as was prevalence in smooth target surface (El-jummah et al., 2016a,). The result of this lack of interaction between the jets with obstacles is that lower turbulence and lower HTC are expected, as shown in Figure 8 (left).

3.5   Thermal Gradients in the Target and Fin Walls

The complex aerodynamics of impingement jets array with a narrow gap, is that there is a flow reversal on the centreline between each group of 4 holes in a square array, as in Figure 11 (left: a - d) and is based on Equation 3: surface distribution of normalised temperature T*. This reverse flow jet is heated by the heat that was transferred from the target surface, as a result of which the heated jet impinges on the jet wall and heats up the impingement surface. Very few experiments by Goldstein et al. (1982a, b) have been made of this component of the heat transfer in impingement cooling. The action of obstacles can be to interfere with this reverse flow jet, particularly if the obstacle is placed where the reverse flow jet occurs, as it was for the co- and cross-flows pins shown in Figure 11 (left). This therefore affects the heat extraction from the target wall as clearly demonstrated by contours of normalized temperature shown in Figure 11 (right: a - d). Therefore, the impingement jet wall will then be heated (not cool) with the heated air as shown by Figure 12 for the surface average HTC on the jet wall. Figure 12 show that as most of the heated air recirculate and heat the jet wall for the cross-flow obstacles. Based on this, there surface average HTC is significantly higher while the dimple gave the lowest HTC

as the heated air concentrates in the dimple. Also showing lower HTC with similar trend to the dimple obstacle is the co-flow obstacle, which was based on the fact that the impingement gap cross-flow takes away most of the heated air, hence lower HTC was observed.

In Figure 11 (left), all the obstacle walls on the target surface shows that the heat transfer is dominated highly on the obstacles, even though for the dimple most of it reversed back to or circulate inside the dimple pot as in Figure 11 (left: d and right: d). A high impingement target surface local HTC will give greater thermal gradients, as it is extracting more heat. The greatest thermal gradient occur in the pins, with the highest gradients in the cross-flow in rectangular pins of Figures 11 (left) and 13 (for the obstacle at the region of hole 9). However, it is heat extraction from the target wall that is required and the thermal gradients here are greatest for the dimple obstacle over the first few rows of impingement jets and it implies better cooling. The trend of the thermal gradient in the obstacle for the cross-flow is similar to that of the co-flow obstacle, even though with little variation in their data. The reason for the these are that for the cross-flow air re-circulation in around the vicinity of the obstacles created better heat extraction on the obstacles, while for the co-flow was mostly the impact of the impingement jet cross-flow in the gap. The heat transfer is significant and is roughly 50 - 60% lower than the impingement target surface average HTC of Figure 9. This has been previously reported by the authors and others (El-jummah et al., 2014a and Xie et al., 2013) and has been shown to influence the effectiveness of the target wall cooling.

4.0   Conclusions

Conjugate heat transfer CFD predictions were used to improve on the efficiency of regenerative wall cooling for low NO_x combustors using obstacles in the impingement gap. A high coolant mass flux G and low pressure loss requires a low impingement X/D and 4.66 was investigated.

The current CHT CFD methodology had been validated using the impingement gap exit pressure loss and the surface average HTC. The CFD validation concentrate on only the rectangular pins in co-flow and cross-flow obstacles, as they are the only obstacles with available experimental data.

The prediction of the thermal gradient in the target wall/obstacles and in the air jet flow, reveals that heat extracted by the air could be the result of the heated jet wall and this reduces the HTC on the target surface. Also shown was that most of the air cooling in the impingement gap were dominated around or within the vicinity of the obstacles, which also affects the target surface and X^2 average HTC as the dominance also impact on the hole flow-maldistribution.

The computational methodology applied in this work indicates that improvement of gas turbine cooling system could be employed, as such the CHT CFD application is adequate for the design analysis of GT cooling geometries. Therefore, this work recommend future enhancing obstacles that could explore both experimental and computational analysis that could provide validation.

Nomenclature

D   Impingement air hole diameter, m

Do   Obstacle diameter, m

G   Coolant Mass flux, kg/sm^2bar

h   Heat transfer coefficient (HTC), W/m^2K

H   Obstacle height, m

k_f Thermal conductivity of fluid, W/mK

Corresponding author's e-mail address: al-jummah@hotmail.com

L	Test wall metal thickness, m
n	Number of jet hole/unit surface area, m^{-2}
N	Number of upstream rows of impingement holes
Nu	Nusselt Number
ρ	Density of air, kg/m^3
ΔP	Impingement wall pressure loss, Pa
P	Coolant supply static pressure (approx. 1bar)
Pr	Prandtl number
Re	Reynolds number
t	Obstacle thickness, m
T_∞	Coolant temperature, K
T^*	Normalized mean temperature
T_S	Target surface metal wall temperature, K
T_w	Target wall imposed temperature (K)
V_j	Impingement jet mean velocity, m/s
U_C	Impingement gap cross-flow velocity, m/s
ν	Kinematic viscosity, m^2/s
W	Obstacle width, m
X	Hole to hole pitch, m
y^+	Inner variable wall normal coordinate ($\xi U\tau/\nu$)
Z	Plate to plate gap, m
ξ	Grid cell size, m
δ	Obstacle depth, m

Subscripts

L	Local
C	cross-flow
h	hole
j	Jet
W	Wall
s	Surface
∞	Coolant
f	fluid
o	Obstacle

References

Abdul Husain, RAA. and Andrews, GE. 1991. Enhanced Full Coverage Impingement Heat Transfer with Obstacle in the Gap. Proceedings of the ASME International Gas Turbine and Aeroengine Congress and Eposition, 91-GT-346, 1 - 12.

El-jummah, AM., Oluwole, FA., Andrews, GE. and Staggs, JEJ. 2017. Numerical Predictions of Enhanced Impingement Jet Cooling with Ribs and Pin Fin in Co-flow and Cross-flow

Configurations. Arid Zone Journal of Engineering, Technology and Environment (AZOJETE), 13 (1): 149 - 162.

El-jummah, AM., Andrews, GE. and Staggs, JEJ. 2018. Enhancement of Impingement Heat Transfer with the Cross-flow Normal to Ribs and Pins between each Row of Holes. Proceedings of the ASME Turbo Expo: Turbomachinery Technical Conference and Exposition, GT - 76969, 1 - 12.

El-jummah, AM., Abdul Hussain, RAA., Andrews, GE. and Staggs, JEJ. 2014a. Conjugate Heat Transfer Computational Fluid Dynamic Predictions of Impingement Heat Transfer: The Influence of Hole Pitch to Diameter Ratio X/D at Constant Impingement Gap Z. Transactions of the ASME: Journal of Turbomachinery, 136 (12): 1 - 16.

El-jummah, AM., Andrews, GE. and Staggs, JEJ. 2016a. Impingement Jet Cooling with Ribs and Pin Fin Obstacles in Co-flow Configurations: Conjugate Heat Transfer Computational Fluid Dynamic Predictions. Proceedings of the ASME Turbo Expo: Turbomachinery Technical Conference and Exposition, GT- 57021, 1 - 15.

El-jummah, A. M., Abdul Hussain, RAA., Andrews, GE. and Staggs, JEJ. 2013. Conjugate Heat Transfer CFD Predictions of the Surface Averaged Impingement Heat Transfer Coefficients for Impingement Cooling with Backside Cross-flow. Proceedings of the ASME IMECE Conference, IMECE-63580, 1 - 14.

El-jummah, AM., Abdul Hussain, RAA., Andrews, GE. and Staggs, JEJ. 2014b. Conjugate Heat Transfer CFD Predictions of Impingement Heat Transfer: Influence of the Number of Holes for a Constant Pitch to Diameter Ratio X/D. Proceedings of the ASME Gas Turbine Conference, GT-25268, 1 - 14.

Xie, Y., Li, P., Lan, J. and Zhang, D. 2013. Flow and Heat Transfer Characteristics of Single Jet Impinging on Dimpled Surface Transactions of the ASME: Journal of Heat Transfer, 135: 1 - 15.

El-jummah, AM., Andrews, GE. and Staggs, JEJ. 2013a. Conjugate Heat Transfer CFD Predictions of Impingement Jet Array Flat Wall Cooling Aerodynamics with Single Sided Flow Exit. Proceedings of the ASME Turbo Expo Conference, GT-95343, 1 - 12.

El-jummah, AM., Andrews, GE. and Staggs, JEJ. 2013b. Conjugate Heat Transfer CFD Predictions of the Influence of the Impingement Gap on the Effect of Cross-Flow. Proceedings of the ASME Heat Transfer Conference, HT-17180, 1 - 12.

El-jummah, AM., Andrews, GE. and Staggs, JEJ. 2015a. Conjugate Heat Transfer CFD Predictions of Metal Walls with Arrays of Short Holes as used in Impingement and Effusion Cooling. Proceedings of the GTSJ International Gas Turbine Congress, IGTC TS - 266, 1 - 9.

El-jummah, AM., Andrews, GE. and Staggs, JEJ. 2015b. CHT/CFD Predictions of Impingement Cooling With Four Sided Flow Exit. Proceedings of the ASME Turbo Expo, GT-42256 1 - 12.

Corresponding author's e-mail address: al-jummah@hotmail.com

El-jummah, AM., Andrews, GE. and Staggs, JEJ. 2016b. Impingement/Effusion Cooling Wall Heat Transfer: Conjugate Heat Transfer Computational Fluid Dynamic Predictions. Proceedings of the ASME Turbo Expo: Turbomachinery Technical Conference and Exposition, GT-56961, 1 - 14.

El-jummah, AM., Andrews, GE. and Staggs, JEJ. 2019. Predictions of Impingement Heat Transfer with Dimples, Pin-fins and zig-zag rib Obstacles: Conjugate Heat Transfer Computational Fluid Dynamics Predictions. Proceedings of ASME Turbo Expo: Turbomachinery Technical Conference and Exposition, GT-90730, 1 -12.

Goldstein, RJ. and Taylor, JR. 1982b. Mass Transfer in the Neighbourhood of Jets Entering a Cross-Flow. Transactions of the ASME: Journal of Heat Transfer, 104: 715 - 721.

Oldstein, RJ. and Timmers, JF. 1982a. Visualization of Heat Transfer from Arrays of Impinging Jets. Pergamon International Journal of Heat and Mass Transfer, 25 (12): 1857 - 1868.